Deep Subsurface Water Stores Sustain Giant Sequoias

Benjamin Eppinger
beppinger@vt.edu

Virginia Tech

W. Holbrook
Virginia Tech https://orcid.org/0000-0003-0065-8841

Dario Grana
University of Wyoming https://orcid.org/0000-0003-4220-053X

Clifford Riebe
University of Wyoming https://orcid.org/0000-0002-8744-8208

Claire Lukens
Universty of California, Merced

Anthony Ambrose
Ancient Forest Society

Sean Bemis
Virginia Tech https://orcid.org/0000-0001-7854-6394

Denise Burgett
Virginia Tech

Anya Gupta
Virginia Tech

Shiv Gupta
Virginia Tech

Article

Keywords:

Posted Date: December 16th, 2025

DOI: https://doi.org/10.21203/rs.3.rs-8060016/v1

Additional Declarations: There is **NO** Competing Interest.

Deep Subsurface Water Stores Sustain Giant Sequoias

Benjamin J. Eppinger[1], W. Steven Holbrook[1], Dario Grana [2], Cliff S. Riebe [2], Claire E. Lukens [3], Antony R. Ambrose[4], Sean P. Bemis[1], Denise Burgett[1], Anya R. Gupta[1], Shiv M. Gupta[1]

[1]Department of Geosciences, Virginia Polytechnic Institute and State University, Blacksburg, VA, USA

[2]Department of Geology and Geophysics, University of Wyoming, Laramie, WY, USA

[3]Department of Life and Environmental Sciences and Sierra Nevada Research Institute, University of California Merced, Merced, California, USA

[4]Ancient Forest Society, South Lake Tahoe, CA, USA

Abstract

Giant sequoias (*Sequoiadendron giganteum)* are adapted to a narrow ecological niche where they endure long, dry summers, during which their water use may exceed ~2 m^3/day. To meet this demand, sequoias rely on subsurface water stores, the volume and distribution of which remains uncharacterized. Here we use hydrogeophysics to quantify subsurface water content in the Mariposa Grove of Giant Sequoias in Yosemite National Park. We use elastic full-waveform inversion to constrain P- and S-wave velocities, then apply a geostatistical rock physics inversion to estimate porosity and water saturation. Our results show broad zones of high water content within the upper 2 m of the subsurface near drainages, whereas on hillslopes and ridges, areas of high water content tend occur in deeper or in more isolated zones. Additional analysis of the water content models shows that in order to avoid water stress throughout the summer, hillslope and ridgetop sequoias probably access substantial volumes of deep (> 2 m) rock moisture from weathered bedrock, implying that the extensive rooting systems of giant sequoias probe deeper into the subsurface than previously thought.

Main Text

As the world's largest trees by mass, giant sequoias have substantial ecological, cultural, and economic importance, as they rapidly sequester carbon [1], contain millennial records of climate [2], and draw millions of visitors [3]. Giant sequoias have a restrictive natural range, occupying only a narrow elevation band (1,400-2,400 m) of the western Sierra Nevada, where a Mediterranean climate produces long, dry summers and temperate winters. During the summers, forest fires enable sequoias to reproduce by opening their cones, whereas during the winters, large volumes of snowfall accumulate, later melting and supplying recharge to subsurface water stores [4]. This cycle of winter snow and summer fire is not only rare, but also delicate, and contemporary environmental change threatens to restrict sequoia habitats further [5]. For example, during the 2012-2016 California drought, diminished snowfall and hotter, drier summers resulted in significant sequoia dieback [6].

Giant sequoias are vulnerable to drought due to their high water demand, as mature trees require up to 2 m^3 of water per day during peak photosynthesis [7]. Moreover, the months-long dry period during the summer means sequoias lack access to significant sources of atmospheric moisture, and therefore must rely on soil and rock moisture [4,8]. Despite giant sequoia resilience and survival being linked to subsurface water stores, below-ground data from sequoia habitats are sparse, generally limited to soil moisture measurements in the upper meter [8]. As a result, little is known about how much subsurface water giant sequoias can access, what depths it resides at, and how vulnerable it might be to drought and environmental change.

To address this knowledge gap, we characterize subsurface structures and quantify below-ground water stores by applying two geophysical techniques. The first is time-frequency-phase, full waveform inversion (FWI), which constrains P-wave velocity (Vp) and S-wave velocity (Vs) from seismic data [9,10]. The second is a geostatistical rock physics inversion that estimates porosity and saturation from seismic velocities, thereby providing estimates of volumetric water content throughout the subsurface [11]. We apply these methods in the Mariposa Grove of Giant Sequoias within Yosemite National Park, California, USA, which is home to over 500 mature giant sequoias [3]. Our study consists of three geophysical profiles (Figure 1), all of which are located within a 0.1 km^2 area mantled by sandy soils derived from the weathering of the underlying meta-volcanic bedrock [12]. While the profiles span a variety of landscape positions and topographic wetness index (TWI) values, climate and underlying geology are constant.

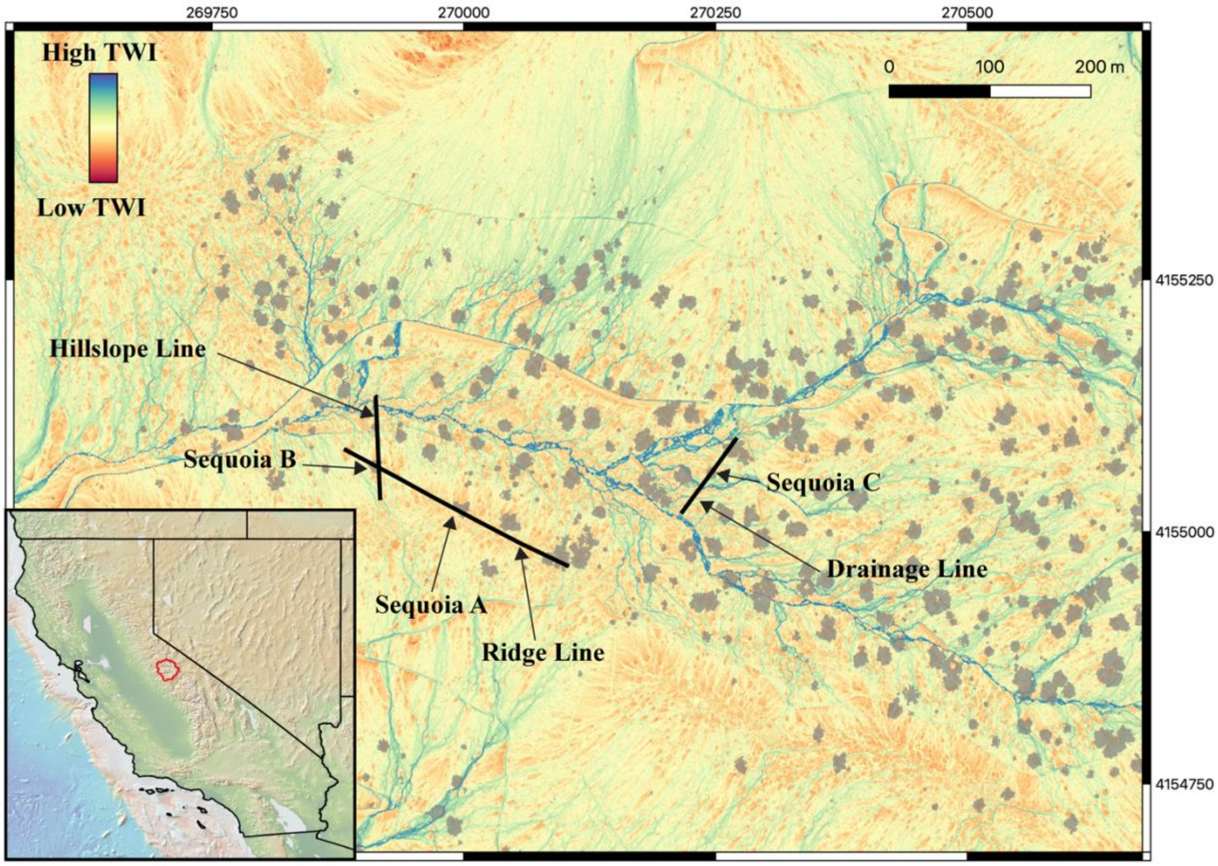

Figure 1: The bottom left inset shows the bounds of Yosemite National Park marked in red within California, USA. The primary map shows a section of the Mariposa Grove within Yosemite. Several giant sequoias lie along the geophysical profiles, and many more sequoia crowns within the study area can be seen via a canopy height map (first return lidar digital elevation model (DEM) minus bare earth lidar DEM), filtered to show tree canopy 55 m and taller in gray. The three mature giant sequoias studied here are labeled, A, B and C. Solid black

lines are the three geophysical profiles from this study, with one profile located upon a ridge (Ridge Line), another descending a hillslope (Hillslope Line), and a third within a drainage (Drainage Line). Colors indicate the topographic wetness index (TWI) computed using the recipe from [13] and a 0.5 m resolution digital elevation model.

Geophysical Imaging of Subsurface Structures and Water Stores

By combining the full waveform inversion velocity models with aerial and handheld lidar derived point clouds, we create a series of images spanning treetop to bedrock (Figure 2). The FWI models reveal a heterogeneous subsurface structure, with greater variability observed in the S-wave velocity models than in the P- wave velocity models (as expected given the shorter wavelengths of shear waves). Across our study site, the depth to weathered bedrock, marked by velocities of ~1200 m/s in Vp [14], varies significantly across the profiles from 1 to 20 m. The ridge profile has a thicker mantle of soil and saprolite, while the soil and saprolite are thinner along the drainage profile, which shows high-velocity, intact bedrock within 20 m of the surface. Along the hillslope profile, the depth to weathered bedrock tends to decrease from the ridge top to valley bottom. Several giant sequoias taller than 50 m lie along the profiles, including four along the ridge line and two along each of the hillslope and drainage lines. The spacing of giant sequoias in the vicinity of the ridge line appears to be less dense than around the hill slope and drainage lines (Figures 1 and 2).

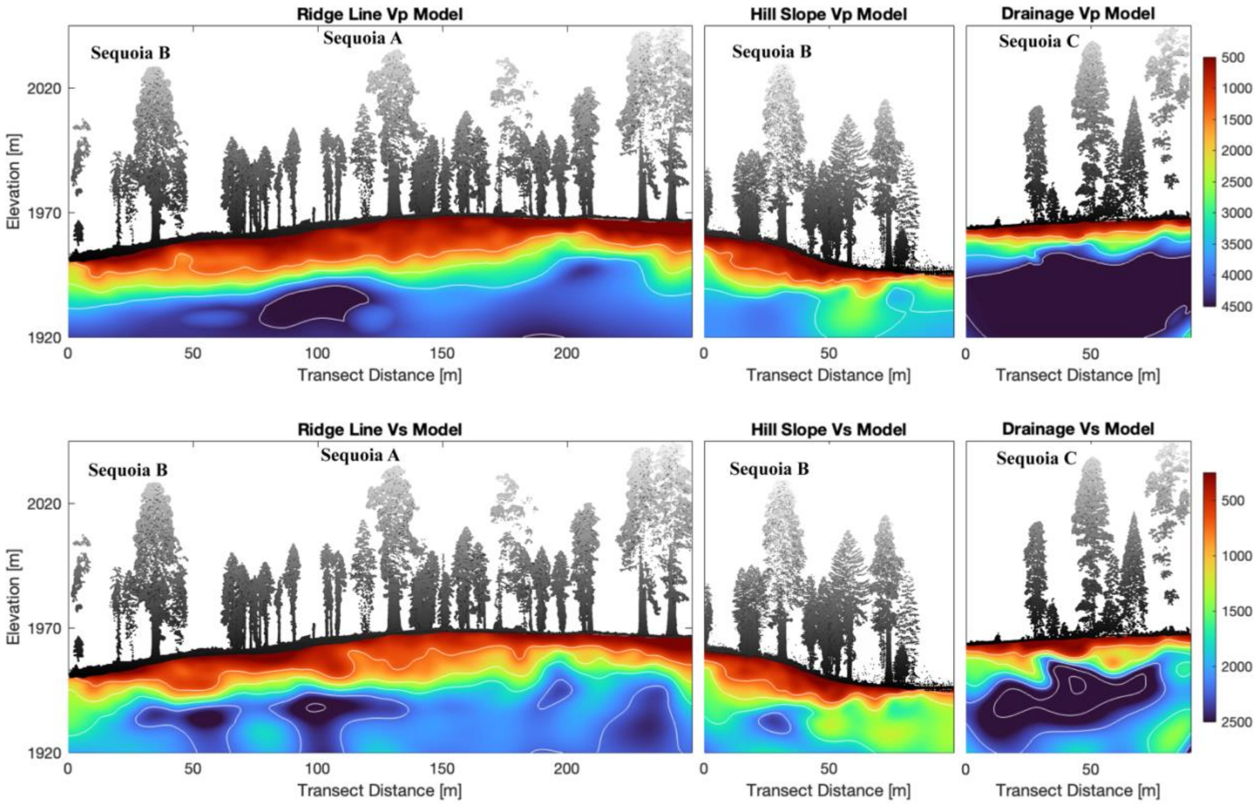

Figure 2: Full waveform inversion seismic velocity models of the subsurface beneath giant sequoias from the three profiles demarcated in Figure 1: The ridge, hillslope, and drainage lines. The giant sequoias labeled in Figure 1 are also labeled in this figure. The top row shows P-wave velocity models with white velocity contours at 1,000 m/s increments. The bottom row displays S-wave velocity models with white velocity contours at 500 m/s increments. Each subplot represents a 2D cross-section of the subsurface, with elevation on the vertical-axis and transect distance on the horizontal. The color scale indicates seismic velocity in meters per second, with warmer colors corresponding to lower velocities and cooler colors corresponding to higher ones. Above of the tomograms are 10 m wide swaths of airborne and handheld lidar point clouds centered on the seismic lines, depicting the position and scale of the overlying vegetation.

The geostatistical rock physics inversion uses the FWI velocity models (Figure 2) to predict hydrological variables. While the predicted porosity field shows similar spatial patterns to the velocity models, the predicted saturation fields are more related to the Vp-Vs ratios (Extended Data Figure 1). Taking the product of the porosity and saturation fields yield the volumetric water content models shown in Figure 3. The Ridge Line water content model shows thick zones of dry material blanketing the highest elevation areas of the profile. However, at lower elevations towards the beginning of the Ridge Line, distinct zones of wetter material extend towards the surface. Along the hillslope line, a superficial layer of dry material thins from the hilltop to the valley and disappears at the bottom of the profile, where a zone of relatively high soil moisture reaches the surface. The drainage profile contains multiple shallow zones of high water content underlain by low-porosity bedrock, which holds little water despite being saturated. In both the hillslope and drainage profiles, there is less woody vegetation in the wettest and lowest elevation areas (Figures 1 and 3), which may be too wet to be suitable for trees.

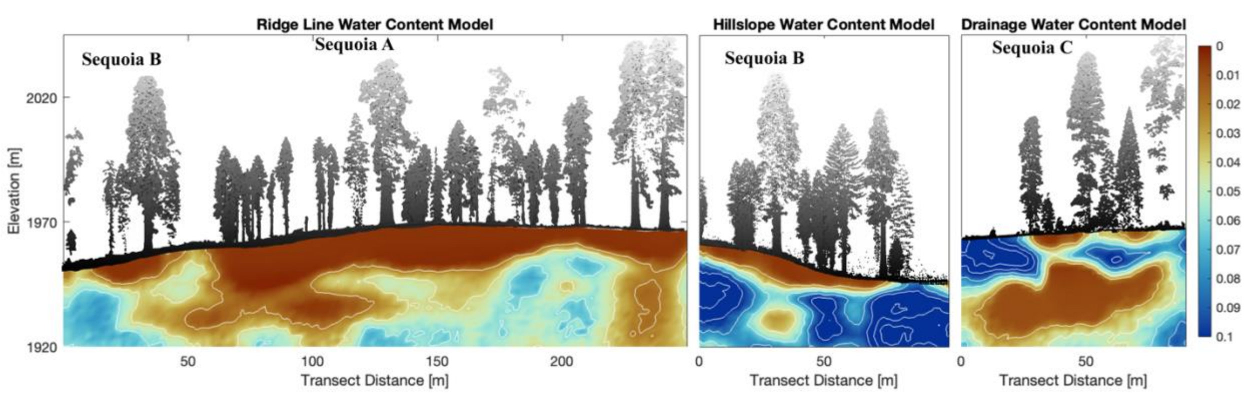

Figure 3: Volumetric water content models (as a fraction of total volume) for the three profiles in Figure 1, derived by multiplying the geostatistical porosity and saturation models. The giant sequoias labeled in Figure 1 are also labeled in this figure. Cooler colors show wetter areas while warmer colors show drier ones. The white contour lines show 0.02 increments of water content.

The three geophysical profiles show that sequoia growth patterns correlate with spatial variability in subsurface water content across the grove, such that sequoias grow densely near shallow zones of high water content in drainages or toward the bottom of hillslopes (Figures 1 and 3). On ridges, in contrast, sequoias appear to grow in patchy stands underlain by commensurately patchy zones of deep rock moisture. Broadly speaking, the hydrogeophysical results affirm that the depth and quantity of subsurface moisture is strongly influenced by landscape position [15,16]. However, these models also quantify volumetric water content throughout the subsurface and reveal heterogeneities in subsurface structure and water stores that cannot be predicted from landscape position alone.

Where Do Giant Sequoias Source Their Water From?

We currently do not know where sequoias source their water from, in part, because sequoia rooting habits are not well understood. While peer-reviewed observations are rare, previous studies report that mature sequoia roots may only laterally extend 15 m near surface water, yet typically extend up to 30 m in well drained soils [17]. Variability in sequoia lateral rooting extent suggests these trees adapt their roots according to available water stores. Rooting depth is poorly known: while it is widely reported that sequoias develop dense root systems in the upper meter of soil [4,17], reports exist of sequoia roots going as deep as 14 m (Todd E. Dawson, personal communication, December, 2023). Our models of subsurface water content (Figure 3) allow estimates of available subsurface water for a range of rooting scenarios, from which we can infer which portions of the subsurface hold sufficient moisture for sequoias to avoid water stress during the dry season.

We compute available subsurface water within sequoia rooting zones as a function of rooting lateral extent and depth by integrating the water content models (Figure 3) over a set of rooting scenarios, spanning 0-80 m in lateral rooting extent and 0-20 m in rooting depth (see the methods section for more details). These results can be seen in Figure 4 but should be taken with the caveat that we do not account for three-dimensional variability or factors diminishing the amount of subsurface water extracted by sequoias, such as limited root density, low soil water potential, and competition with other plants. Therefore, this analysis provides a conservative upper-bound for extractable subsurface water at the time of the seismic surveys. Given that the seismic data was collected in late July to early August of 2023 and 2024, the water volumes detected through the geophysical surveys represent the amount remaining with ~100 days left in the dry seasons. Between July and October of both 2023 and 2024 the Mariposa Grove received less than an inch of precipitation [18,19]. Therefore, each giant sequoia tree would require ~200 m^3 of subsurface water from the time of our seismic surveys to avoid water stress [7]. This approximation does not account for sequoias adapting their water use as subsurface stores are depleted. Nevertheless, the 200 m^3 estimate provides a reasonable starting point to assess the feasibility of different rooting scenarios, and other water requirement scenarios can also be assessed with Figure 4.

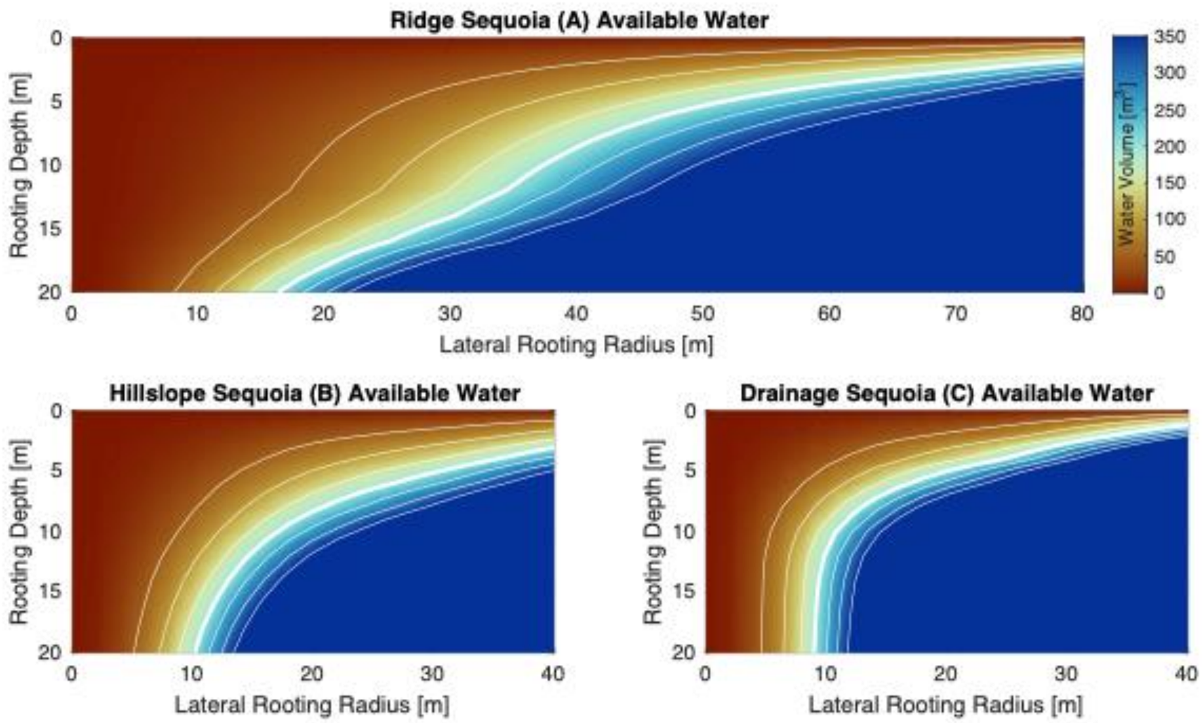

Figure 4: Available subsurface water volumes for the three giant sequoias labeled in Figures 1, 2, and 3: Ridge Line (Sequoia A), Hillslope Line (Sequoia B), and Drainage Line (Sequoia C). Each panel shows the total subsurface water content within a cylindrical volume around each sequoia, as a function of rooting depth (vertical axis) and lateral rooting radius (horizontal axis). Warmer colors represent less available water while cooler colors represent more. Overlying the color plots are available water content contour lines, starting at 50 m^3 and increasing by 50 m^3 increments until 350 m^3. The thick white line is the 200 m^3 contour, which represents the total water a sequoia tree would need to survive 100 precipitation-free days without water stress.

Visualizing total available subsurface water volume as a function of rooting depth and lateral rooting extent shows the feasibility of different rooting strategies for the three sequoias. The sequoia nearest the drainage (sequoia C) has the most readily accessible subsurface water and is the only one of the three trees analyzed that can access more than 200 m^3 of water with roots that extend 35 m laterally but no more than 2 m deep. Therefore, this tree has no apparent need to develop deep roots. In contrast, the giant sequoia along the hillslope line (sequoia B) must either root down to depths of 4-6 m or laterally extend its roots greater than 40 m to access adequate subsurface water. The sequoia in the middle of the ridge line has the least readily accessible subsurface water. In order for this tree to avoid water stress, it may need to root to depths exceeding 8 m or at lateral extents exceeding 75 m. The results from Sequoias A and B show that in order to access adequate subsurface water, certain sequoias may need to grow deeper, or more extensive lateral roots than previously thought, raising the question of which is more likely. While the extensive shallow roots of giant sequoias are commonly cited, here we argue that deep (> 2 m depth) roots are also vital.

Our geophysical results and analysis provide evidence that deep roots may be necessary for some sequoias due to the dry summer soil conditions on ridges and hillslopes. This is reflected in the water content models showing that at higher landscape positions, shallow soil moisture is lacking while deep rock moisture is present (Figure 3). To adapt to these hydrological conditions, sequoias can reduce the root volume needed to access 200 m^3 of water by growing roots deeper than 2 m (Figure 4). Stable hydrogen and oxygen isotope ratios measured in xylem water from sequoias in Giant Forest (Sequoia National Park), Merced grove (Yosemite National

Park), and Mariposa grove (Yosemite National Park) also suggest sequoias root deeper than 2 m. (A. Ambrose, unpublished data). In a broader sense, these findings concur with observations of trees in Mediterranean climates growing roots deeper than 10 m to access subsurface water [20] as well as with hydrological models suggesting that rock moisture sustains a large portion of woody vegetation across the western United States [21].

The reliance of giant sequoias and many other plant species on deep subsurface water underscores the ecological importance of soil/rock moisture housed in saprolite and weathered bedrock [21–23]. Geophysical imaging results presented here (Figure 2) and elsewhere [24,25] have shown these regions of the subsurface to be spatially heterogenous. We hypothesize that small-scale variations in the structure of saprolite, fractured bedrock, and the rock moisture therein can help explain patchy forest dieback during drought [6]. If so, geophysical imaging and rock physics modeling can provide tools for forest managers contending with the worsening effects of severe droughts [26].

Extended Data

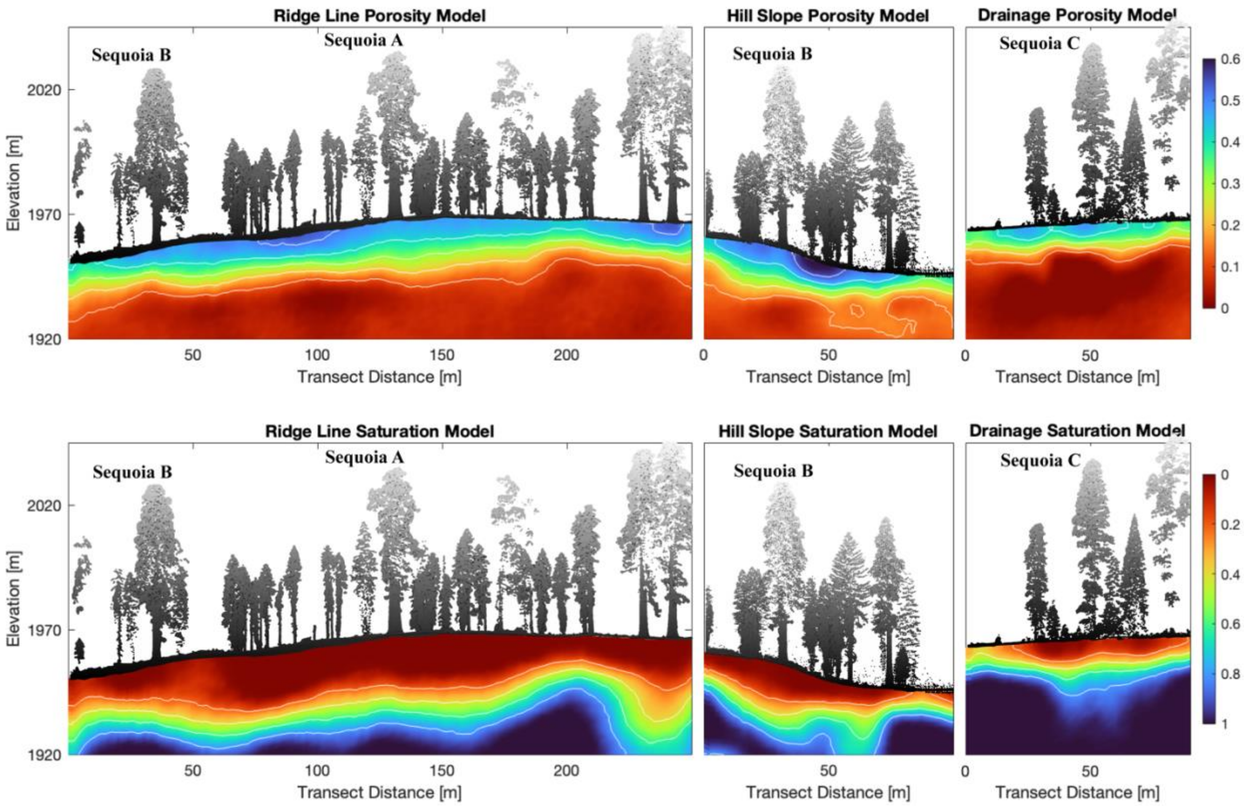

Extended Data, Figure 1: Geostatistical rock physics inversion results from the three different profiles demarcated in Figure 1. The giant sequoias labeled in Figure 1 are also labeled in this figure. The top row shows porosity models with white contours at 0.1 increments, with cooler colors showing more porous material. The bottom row shows saturation models with white contours at 0.2 m/s increments, with cooler colors showing more saturated material. Overlying each cross-section are vegetation point clouds derived from handheld and aerial lidar measurements.

Profile	Date Collected	Vertical Component	Horizontal Component	Geophone Spacing	Source Spacing
Ridge Line	1 Aug 2023	Yes	Yes	0.5 m	5 m
Hillslope Line	22 Jul 2024	Yes	No	0.2 m	1 m
Drainage Line	25 Jul 2023	Yes	No	0.25 m	2 m

Extended Data, Table 1: acquisition parameters for seismic surveys.

Methods

Geophysical Data Acquisition

The seismic refraction data were collected along linear profiles of autonomous Stryde accelerometer nodes using a sledgehammer and aluminum plate to excite seismic energy. See extended data table 1 for the acquisition details of each of the seismic surveys. Following data collection, we integrated the shot records twice with respect to time to create displacement seismograms. Since low frequency noise in the raw data is boosted by time integration, before integrating, we applied a 5-65 Hz Ormsby filter to the acceleration data. Prior to converting the data from acceleration to displacement, we manually picked and inverted first arrivals using Pygimli's ray-based travel time tomography software [27]. We scaled the resultant Vp models by 0.5 to create initial Vs models for FWI.

Elastic Full Waveform Inversion Using a Time-Frequency-Phase Misfit Functional

Over the past three decades, full waveform inversion (FWI) has become a state-of-the-art method for constraining subsurface properties [28–30]. Emerging applications for FWI include exploring the upper ~50 m of Earth's subsurface, also known as the critical zone (CZ), where bedrock weathers and becomes soil [24,25]. Compared to classical seismic methods used for CZ imaging, such as first arrival travel time tomography, FWI can constrain higher resolution Vp and Vs models if a suitable misfit functional is chosen and proper data preconditioning techniques are employed [25,31–35]. CZ structure is characterized by extreme velocity gradients (with velocities spanning the interval of 150-6000 m/s), ample heterogeneity, and a mixture of material properties ranging from very soft soil to very stiff intact bedrock. This makes the amplitude response of CZ seismic data complex and difficult to recover with synthetic modeling. Past work implementing FWI in the CZ has therefore tended toward fitting phase information [24,25,36–38].

In this work, we use a misfit functional for CZ FWI designed to match the phase of synthetic and observed data. The misfit functional was originally developed with time frequency analysis based on the Gabor transform [9], but we have adapted it by using the continuous wavelet transform (CWT) for our time-frequency analysis. The CWT is better suited for CZ FWI because its adaptive windowing function leads to enhanced time-frequency resolution over a wider frequency range [39]. This helps contend with the rapidly changing frequency content and broad band nature of CZ seismic data.

Before performing FWI, we estimated unique source-time functions at each hammer-swing location using stabilized deconvolution [40,41]. During the FWI, we applied data preprocessing by filtering and muting the record sections. We followed other work implementing FWI for CZ study by designing muting windows that would focus the inversion on primarily fitting body waves [25]. We also employed a Butterworth bandpass filter to implement a classical frequency continuation multiscale strategy [42]. We sequentially inverted data in frequency bands of 5-20 Hz, 5-35 Hz, 5-50 Hz, and 5-65 Hz, which helped improve convergence and avoid local minima. To iteratively update the earth models, we computed gradients with respect to the time-frequency-phase misfit function using the adjoint method and the open source specfem2d software [43,44]. For inversions at each frequency band, we enforced regularity by convolving the gradients with two-dimensional Gaussian functions [45]. In the supplementary information we provide more mathematical and technical details about the CWT and our FWI method. We also provide results from synthetic tests verifying our approach and providing insights into the expected resolution of the surveys.

Geostatistical Rock Physics Inversion for Predicting Porosity and Saturation

While FWI can constrain high-resolution Vp and Vs models, these properties are usually not of immediate interest to non-geophysicists. Rock physics models can be used to relate geophysical properties to hydrological ones [46]. Previous studies have used rock physics models to estimate the water holding capacity of the CZ from Vp tomograms [24,47]. Moreover, geostatistical data assimilation methods can be combined with rock physics models to estimate saturation from seismic data [48–50]. In this work, we employ a variant of a previously published geostatistical rock physics inversion algorithm[11] to estimate porosity and saturation from FWI Vp and Vs models.

For the rock physics inversion, we first generate an initial ensemble of porosity and saturation models. We do this using the probability field simulation method [51] and impose horizontal and lateral smoothing throughout to enforce spatial regularization. We also mandate that in the initial ensemble, porosity monotonically decreases while saturation monotonically increases with depth, which reflects the fact that less weathered and more saturated materials tend to occur deeper in the CZ. To relate the porosity and saturation realizations to Vp and Vs, we use a combined empirical and theoretical rock physics model. The model is empirical in the sense that we use exponential functions to relate porosity to dry values of Vp and Vs, and theoretical in that we use Gassmann's equation [46] to compute the effect of saturation on the seismic velocities. This approach is well suited for our study because the empirical model can account for the wide range of seismic velocities in the CZ better than other rock physics models such as Berryman's inclusion model [52] or Dvorkin and Nur's [53] soft sand model. The final step of our rock physics inversion is to use the ensemble smoother algorithm [54] to update the porosity and saturation realizations to be more consistent with the Vp and Vs tomograms. In the supplementary information, we provide more mathematical background and technical details about the rock physics model and inversion.

Computing Maximum Subsurface Water Volumes

To calculate the maximum subsurface water volume accessible for giant sequoias located along our geophysical transects, we begin by laterally extruding the porosity and saturation models in the direction perpendicular to the trend of the profiles. Then, assuming that the roots grow in a cylinder with a radius equal to the lateral rooting extent, we integrate the product of porosity and saturation within the cylinder to compute the total available water volume. We repeat this for each rooting lateral extent and depth scenario. To account for topography, prior to integrating, we re-datum the porosity and saturation models to replace the elevation axis with depth.

References

1. Sillett, S. C., Van Pelt, R., Carroll, A. L., Campbell-Spickler, J. & Antoine, M. E. Structure and dynamics of forests dominated by Sequoiadendron giganteum. *Forest Ecology and Management* **448**, 218–239 (2019).
2. Hughes, M. K. & Brown, P. M. Drought frequency in central California since 101 B.C. recorded in giant sequoia tree rings. *Climate Dynamics* **6**, 161–167 (1992).
3. Shiflett, S. A., Jenkins, J. S., Mattos, R. F., Ibsen, P. C. & Athearn, N. D. Sequoia Groves of Yosemite: Visitor Use and Impact Monitoring. *Forests* **15**, 2256 (2024).
4. Hartesveldt, R., Harvey, T. & Shellhammer, H. *The Giant Sequoia of the Sierra Nevada*. (U.S. Department of the Interior National Park Service, 1975).
5. Eckmann, T. *et al.* Measuring and modeling microclimate impacts of Sequoiadendron giganteum. *Sustainable Cities and Society* **38**, 509–525 (2018).
6. Stephenson, N. L. *et al.* Patterns and correlates of giant sequoia foliage dieback during California’s 2012–2016 hotter drought. *Forest Ecology and Management* **419–420**, 268–278 (2018).
7. Ambrose, A. R. *et al.* Hydraulic constraints modify optimal photosynthetic profiles in giant sequoia trees. (2016).
8. Rundel, P. W. Habitat Restriction in Giant Sequoia: The Environmental Control of Grove Boundaries. *American Midland Naturalist* **87**, 81 (1972).
9. Fichtner, A., Kennett, B. L. N., Igel, H. & Bunge, H.-P. Theoretical background for continental- and global-scale full-waveform inversion in the time-frequency domain. *Geophysical Journal International* **175**, 665–685 (2008).

10. Fichtner, A., Kennett, B. L. N., Igel, H. & Bunge, H.-P. Full seismic waveform tomography for upper-mantle structure in the Australasian region using adjoint methods. *Geophysical Journal International* **179**, 1703–1725 (2009).
11. Grana, D. *et al.* Geostatistical Rock Physics Inversion for Predicting the Spatial Distribution of Porosity and Saturation in the Critical Zone. *Math Geosci* **54**, 1315–1345 (2022).
12. King, H., Paul, B. & Clyde, W. Geologic Map of Yosemite National Park and Vicinity, California. (1989).
13. van der Kwast, H. & Menke, K. *QGIS for Hydrological Applications: Recipes for Catchment Hydrology and Water Management*. (Locate Press, 2019).
14. Flinchum, B. A. *et al.* Low V_p/V_s Values as an Indicator for Fractures in the Critical Zone. *Geophysical Research Letters* **51**, e2023GL105946 (2024).
15. Condon, L. E. & Maxwell, R. M. Evaluating the relationship between topography and groundwater using outputs from a continental-scale integrated hydrology model. *Water Resources Research* **51**, 6602–6621 (2015).
16. Mata-González, R., Averett, J. P., Abdallah, M. A. B. & Martin, D. W. Variations in Groundwater Level and Microtopography Influence Desert Plant Communities in Shallow Aquifer Areas. *Environmental Management* **69**, 45–60 (2022).
17. Weatherspoon, C. P. Sequoiadendron giganteum (Lindl.) Buchholz Giant Sequoia. (1990).
18. Monthly Precipitation Summary Water Year 2023. California Nevada River Forecast Center (2023).
19. Monthly Precipitation Summary Water Year 2024. California Nevada River Forecast Center (2024).

20. Canadell, J. *et al.* Maximum rooting depth of vegetation types at the global scale. *Oecologia* (1996).
21. McCormick, E. L. *et al.* Widespread woody plant use of water stored in bedrock. *Nature* **597**, 225–229 (2021).
22. Hahm, W. J. *et al.* Lithologically Controlled Subsurface Critical Zone Thickness and Water Storage Capacity Determine Regional Plant Community Composition. *Water Resources Research* **55**, 3028–3055 (2019).
23. Rempe, D. M. & Dietrich, W. E. Direct observations of rock moisture, a hidden component of the hydrologic cycle. *Proc. Natl. Acad. Sci. U.S.A.* **115**, 2664–2669 (2018).
24. Eppinger, B. J., Holbrook, W. S., Liu, Z., Flinchum, B. A. & Tromp, J. 2D Near-Surface Full-Waveform Tomography Reveals Bedrock Controls on Critical Zone Architecture. *Earth and Space Science* **11**, e2023EA003248 (2024).
25. Liu, X., Zhu, T. & Hayes, J. Critical Zone Structure by Elastic Full Waveform Inversion of Seismic Refractions in a Sandstone Catchment, Central Pennsylvania, USA. *JGR Solid Earth* **127**, e2021JB023321 (2022).
26. Ambrose, A. R. *et al.* Leaf- and crown-level adjustments help giant sequoias maintain favorable water status during severe drought. *Forest Ecology and Management* (2018).
27. Rücker, C., Günther, T. & Wagner, F. M. pyGIMLi: An open-source library for modelling and inversion in geophysics. *Computers & Geosciences* **109**, 106–123 (2017).
28. Fichtner, A. *et al.* Seismic Tomography 2024. *Bulletin of the Seismological Society of America* **114**, 1185–1213 (2024).

29. Tromp, J. Seismic wavefield imaging of Earth's interior across scales. *Nat Rev Earth Environ* **1**, 40–53 (2019).
30. Virieux, J. & Operto, S. An overview of full-waveform inversion in exploration geophysics. *GEOPHYSICS* **74**, WCC1–WCC26 (2009).
31. Cai, A. & Zelt, C. A. Early arrival waveform inversion using data uncertainties and matching filters with application to near-surface seismic refraction data. *GEOPHYSICS* **87**, R465–R486 (2022).
32. Groos, L., Schäfer, M., Forbriger, T. & Bohlen, T. The role of attenuation in 2D full-waveform inversion of shallow-seismic body and Rayleigh waves. *GEOPHYSICS* **79**, R247–R261 (2014).
33. Groos, L., Schäfer, M., Forbriger, T. & Bohlen, T. Application of a complete workflow for 2D elastic full-waveform inversion to recorded shallow-seismic Rayleigh waves. *GEOPHYSICS* **82**, R109–R117 (2017).
34. Köhn, D. *et al.* Comparison of time-domain SH waveform inversion strategies based on sequential low and bandpass filtered data for improved resolution in near-surface prospecting. *Journal of Applied Geophysics* **160**, 69–83 (2019).
35. Schwardt, M. *et al.* Characterization of silty to fine-sandy sediments with SH waves: full waveform inversion in comparison with other geophysical methods. *Near Surface Geophysics* **18**, 217–248 (2020).
36. Li, J., Hanafy, S. & Schuster, G. Wave-Equation Dispersion Inversion of Guided *P* Waves in a Waveguide of Arbitrary Geometry. *JGR Solid Earth* **123**, 7760–7774 (2018).
37. Li, J., Feng, Z. & Schuster, G. Wave-equation dispersion inversion. *Geophys. J. Int.* **208**, 1567–1578 (2017).

38. Liu, Z., Li, J., Hanafy, S. M. & Schuster, G. 3D wave-equation dispersion inversion of Rayleigh waves. *GEOPHYSICS* **84**, R673–R691 (2019).

39. Radad, M., Gholami, A. & Siahkoohi, H. R. S-transform with maximum energy concentration: Application to non-stationary seismic deconvolution. *Journal of Applied Geophysics* **118**, 155–166 (2015).

40. Aktharuzzaman, M., Anwar, S., Borisov, D. & He, J. Experimental full waveform inversion for elastic material characterization with accurate transducer modeling. *Mechanical Systems and Signal Processing* **213**, 111320 (2024).

41. Pratt, R. G. Seismic waveform inversion in the frequency domain, Part 1: Theory and verification in a physical scale model. *GEOPHYSICS* **64**, 888–901 (1999).

42. Bunks, C., Saleck, F., Zalesky, S. & Chavent, D. multiscale seismic waveform inversion. *GEOPHYSICS* (1995).

43. Komatitsch, D. & Tromp, J. Introduction to the spectral element method for three-dimensional seismic wave propagation. *Geophys. J. Int.* **139**, 806–822 (1999).

44. Tromp, J., Tape, C. & Liu, Q. Seismic tomography, adjoint methods, time reversal and banana-doughnut kernels: Seismic tomography, adjoint methods, time reversal and banana-doughnut kernels. *Geophysical Journal International* **160**, 195–216 (2004).

45. Modrak, R. & Tromp, J. Seismic waveform inversion best practices: regional, global and exploration test cases. *Geophys. J. Int.* **206**, 1864–1889 (2016).

46. Mavko, G. *The Rock Physics Handbook: Tools for Seismic Analysis of Porous Media*. (Cambridge University Press, 2009).

47. Hayes, J. L., Riebe, C. S., Holbrook, W. S., Flinchum, B. A. & Hartsough, P. C. Porosity production in weathered rock: Where volumetric strain dominates over chemical mass loss. *Sci. Adv.* **5**, eaao0834 (2019).

48. Azevedo, L. & Soares, A. *Geostatistical Methods for Reservoir Geophysics*. (Springer International Publishing, Cham, 2017). doi:10.1007/978-3-319-53201-1.

49. Grana, D. & de Figueiredo, L. SeReMpy: Seismic reservoir modeling Python library. *GEOPHYSICS* **86**, F61–F69 (2021).

50. Flinchum, B. A. *et al.* Estimating the water holding capacity of the critical zone using near-surface geophysics. *Hydrological Processes* **32**, 3308–3326 (2018).

51. Srivastava, R. Reservoir characterization with probability field simulation. (1992).

52. Mixture Theories for Rock Properties. 205–228 (1995) doi:10.1029/rf003p0205.

53. Dvorkin, J. & Nur, A. Elasticity of high-porosity sandstones: Theory for two North Sea data sets. *GEOPHYSICS* **61**, 1363–1370 (1996).

54. Emerick, A. A. & Reynolds, A. C. Ensemble smoother with multiple data assimilation. *Computers & Geosciences* **55**, 3–15 (2013).

Supplementary Files

This is a list of supplementary files associated with this preprint. Click to download.

- DeepSubsurfaceWaterStoresSustainGiantSequoiasSupplementalinfo.pdf